Journal of Materials Science & Technology 191 (2024) 1–7

Contents lists available at ScienceDirect

Journal of Materials Science & Technology

journal homepage: www.elsevier.com/locate/jmst

Research Article

Ultrafast nanomanufacturing via high-temperature shock of $La_{0.6}Sr_{0.4}CoO_3$ catalysts for overall water splitting

Xiaoya Cui [a], Wenyu Li [b], Yanchang Liu [a], Yumei Zhu [b], Yanan Chen [a,*], Cairong Gong [b,*], Gang Xue [c,*]

[a] School of Materials Science and Engineering, Key Laboratory of Advanced Ceramics and Machining Technology of Ministry of Education, Tianjin Key Laboratory of Composite and Functional Materials, Tianjin University, Tianjin 300072, China
[b] School of Materials Science and Engineering, Institute of New Energy, Tianjin University, Tianjin 300072, China
[c] Key Laboratory of Special Functional Materials for Ecological Environment and Information, Ministry of Education, Hebei University of Technology, Tianjin 300132, China

ARTICLE INFO

Article history:
Received 16 August 2023
Revised 15 September 2023
Accepted 15 November 2023
Available online 21 January 2024

Keywords:
Perovskite oxides
High-temperature shock
Water splitting
High Gibbs free energy
Phase engineering

ABSTRACT

Electrochemical water splitting, as an effective sustainable and eco-friendly energy conversion strategy, can produce high-purity hydrogen (H_2) and oxygen (O_2) via hydrogen evolution reaction (HER) and oxygen evolution reaction (OER), respectively, altering the nonrenewable fossil fuels. Here, $La_{0.6}Sr_{0.4}CoO_3$ perovskite oxide nanoparticles with an orthorhombic phase were synthesized within 2 min in a one-step reaction, using a rapid and efficient high-temperature shock (HTS) method. Impressively, the as-prepared $La_{0.6}Sr_{0.4}CoO_3$ with orthorhombic phase (HTS-2) exhibited better OER and HER performance than the hexagonal phase counterpart prepared using the traditional muffle furnace calcination method. The electrocatalytic performance enhancement of orthorhombic $La_{0.6}Sr_{0.4}CoO_3$ can be attributed to the novel orthorhombic structure, such as confined strontium segregation, a higher percentage of highly oxidative oxygen species, and more active sites on the surface. This facile and rapid synthesis technique shows great potential for the rational design and crystal phase engineering of nanocatalysts.

1. Introduction

Hydrogen energy is widely accepted as the most promising substitute for fossil fuels in energy storage and conversion [1–4]. Electrochemical water splitting, involving oxygen evolution reaction (OER) and hydrogen evolution reaction (HER), can produce high-purity oxygen (O_2) and hydrogen (H_2), altering the nonrenewable fossil fuels [5–10]. While noble metal compounds such as ruthenium/iridium oxides (RuO_2/IrO_2) and platinum (Pt) alloys exhibit excellent electrocatalytic performance for both OER and HER, their exorbitant prices make them unsuitable for industrial applications. Thus, researchers are exploring more economical materials with high capacities and stabilities [11–14]. Perovskite oxides, generally with the molecular formula of ABO_3, where A represents alkaline or rare-earth metal and B represents transition metal, could be utilized for electrocatalysis, due to their low cost and tunable crystal structure and physiochemical properties [15–17]. Specifically, the structure variation and the regulation of electronic properties by elemental composition and crystal phase are essential to build the relationship between electronic properties and catalytic performance, and structural evolutions for electrocatalysts [18,19]. For instance, $La_{1-x}Sr_xCoO_3$ ($0 \leq x \leq 1$) oxide is a prevalent type of perovskite, which has been applied as an excellent cathode catalyst for electrical cells and metal-air batteries. Its intrinsic properties for OER and HER reactions are gaining more attention than ever before [20–23]. Liu et al. [24] designed a $LaCoO_3$ /N-doped reduced graphene oxide nanohybrid with improved performances for oxygen reduction reaction (ORR) and OER. Yu et al. [25] reported an Nb-doped $La_{0.4}Sr_{0.6}Co_{0.7}Fe_{0.2}Nb_{0.1}O_3$ bifunctional perovskite, which exhibited superior performance in the aluminum-air battery.

To date, various effective strategies, including solid-phase, co-precipitation, hydrothermal, and sol-gel methods [15,26], have been developed to synthesize functional perovskite oxides, with well-defined size, composition, and morphology. However, it is found that the resulting perovskite oxides tended to be agglomerated with poor specific surface area [25,27]. Therefore, it remains challenging to obtain high-performance perovskite oxides with tunable composition, structure, and crystal phase [28]. Re-

* Corresponding authors.
E-mail addresses: yananchen@tju.edu.cn (Y. Chen), gcr@tju.edu.cn (C. Gong), xuegang@hebut.edu.cn (G. Xue).

https://doi.org/10.1016/j.jmst.2023.11.067
1005-0302/

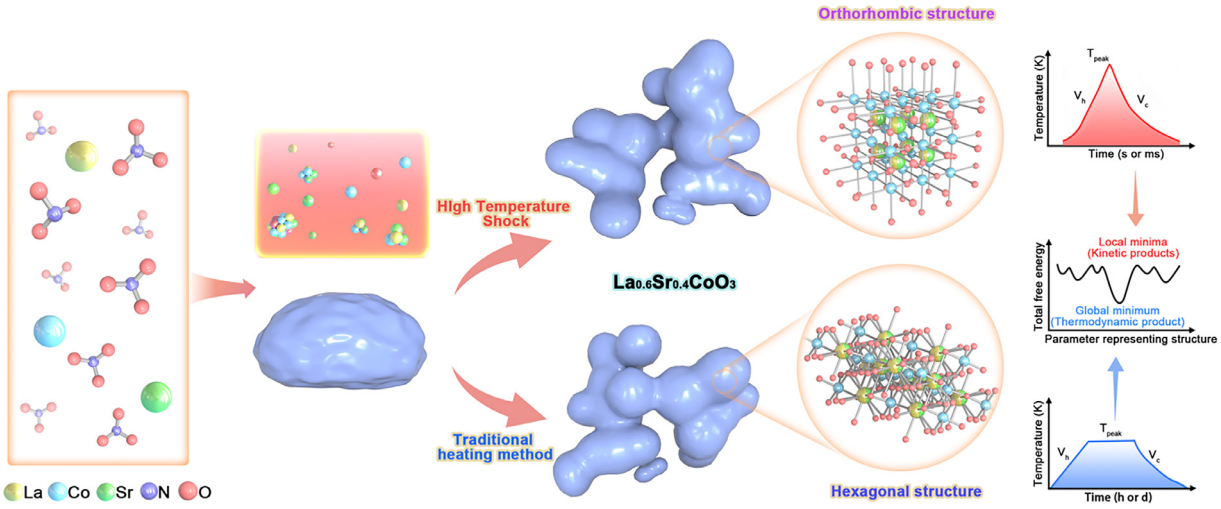

Fig. 1. Schematic illustration of synthesis process for $La_{0.6}Sr_{0.4}CoO_3$ with orthorhombic and hexagonal structures via HTS and traditional heating methods, respectively.

cently, Chen et al. [29] developed a rapid high-temperature shock (HTS) technique, which involves electrical joule heating to achieve ultrahigh reacting temperature with ultrafast heating and cooling rates of 10^5 and 10^4 K s^{-1}, respectively. Notably, the HTS method showed high local temperature over a wide temperature from 300 to 3000 K, which is beneficial for the morphology, structure, and crystal phase modification of well-dispersed nanomaterials with remarkable performances [29–36]. This ultrafast HTS manufacturing method has been used to synthesize various materials, such as monometallic nanoparticles (e.g., Si, Au, Pd, and Ag) [29,37], bimetallic alloy (e.g., NiFe, PdNi, and PtFe) [38,39], and metallic compounds (e.g., SiC, CoS, FeS_2, Co_3O_4, MoS_2, $CoFeP_x$, $LiMn_2O_4$, $LiCoO_2$, $LiFePO_4$, Li-rich layered oxide/NiO heterostructures), etc. [40–44].

In this report, we applied the HTS manufacturing strategy to synthesize $La_{0.6}Sr_{0.4}CoO_3$ perovskite oxides in one step by directly reducing the mixed metal nitrate precursors to the final product, i.e., perovskite oxides at the temperature of up to 1273 K. The process is schematically illustrated in Fig. 1. Note that $La_{0.6}Sr_{0.4}CoO_3$ showed an unusual orthorhombic phase, compared to the hexagonal phase of the bulk counterpart obtained via the traditional heating method. Impressively, the orthorhombic $La_{0.6}Sr_{0.4}CoO_3$ exhibited good HER and OER activities and stabilities. The structure-performance relationship was discussed systematically as well. Phase engineering shows great potential for the modification of structural diversities and catalytic capacity. The reaction mechanism of $La_{0.6}Sr_{0.4}CoO_3$ with different phases for OER and HER is investigated by density functional theory (DFT) calculations to identify the surface reaction pathway. This work offers a facile and rapid method for the synthesis of perovskite oxides with novel crystal phases and excellent electrochemical performance.

2. Results and discussion

2.1. Characterization of morphology and structure

The orthorhombic $La_{0.6}Sr_{0.4}CoO_3$ perovskite oxides were synthesized via a facile, one-step HTS method to heat treat the uniform mixture of $La(NO_3)_3 \cdot 6H_2O$, $Sr(NO_3)_2$, and $Co(NO_3)_2 \cdot 6H_2O$ (Fig. 1, see Experimental section in the Supplementary information for details). A detailed characterization of the as-prepared $La_{0.6}Sr_{0.4}CoO_3$ perovskite oxides is shown in Figs. 2, S1, and S2. The representative high-angle annular dark-field scanning transmission electron microscopy (HAADF-STEM) confirmed the orthorhombic crystal structure of $La_{0.6}Sr_{0.4}CoO_3$ obtained by the HTS method, as compared to the hexagonal structure of that obtained by muffle furnace calcination. Specifically, the lattice distance of $La_{0.6}Sr_{0.4}CoO_3$ obtained by the HTS method is about 0.21 nm (Fig. 2(a)), which is consistent with the orthorhombic phase. In comparison, the lattice distance of the traditional calcinated $La_{0.6}Sr_{0.4}CoO_3$ is about 0.19 nm (Fig. 2(b)) which is aligned to the hexagonal phase. The instant joule heating via HTS may lead the precursors to directly decompose at high temperatures, while the high Gibbs free energy is contained inside the nanoparticles during the ultrafast cooling down process, which is facile to modulate the atomic arrangement, and thus generates defects or unusual crystal phase, i.e., orthorhombic structure for $La_{0.6}Sr_{0.4}CoO_3$. Moreover, the HAADF-STEM and the corresponding energy dispersive X-ray spectroscopy (EDS) elemental mapping images of the orthorhombic $La_{0.6}Sr_{0.4}CoO_3$ showed the uniform distribution of La, Sr, and Co elements, with a La/Sr/Co atomic ratio of 0.26/0.20/0.54 (Figs. 2(c) and S3).

The XRD patterns of the prepared $La_{0.6}Sr_{0.4}CoO_3$ perovskites are shown in Fig. 3(a, b). The diffraction peaks of both catalysts are in correspondence with the standard hexagonal $LaCoO_3$ (PDF#48–0121). Besides, there is an obvious diffraction peak around 31.8° in HTS-2, which indicates the existence of orthorhombic $La_{0.6}Sr_{0.4}CoO_3$ (PDF#46–0704), proving that the orthorhombic perovskite structure was obtained by the HTS method. The muffle-prepared $La_{0.6}Sr_{0.4}CoO_3$ exhibits a peak at 28.8°, aligned to the $SrCO_3$ crystal structure (PDF#74–1491), which might arise from the unconverted precursor in the reaction system. In Fig. 3(b), the diffraction peak at 33.5° of HTS-2 shifted to a smaller angle, indicating that the lattice had expanded a bit more than that obtained by traditional calcination. It could be attributed to the coexistence of orthorhombic structure in $La_{0.6}Sr_{0.4}CoO_3$ (HTS-2), which has a larger lattice parameter, consistent with the HRSTEM results in Fig. 2(a) [45].

To explore the surface area and pore volume of orthorhombic and hexagonal $La_{0.6}Sr_{0.4}CoO_3$, N_2 adsorption/desorption experiments were conducted (Fig. S4). The surface area of orthorhombic $La_{0.6}Sr_{0.4}CoO_3$ was calculated as 21.804 m^2 g^{-1}, larger than that of its hexagonal counterpart (7.000 m^2 g^{-1}), using the Brunauer-Emmett-Teller (BET) model (Table S1). The Barrett-Joiner-Halenda (BJH) pore volume is represented as the inset of Fig. S4, indicating the higher pore volume of ort-$La_{0.6}Sr_{0.4}CoO_3$ (0.098 cm^3 g^{-1}), as compared to hcp one.

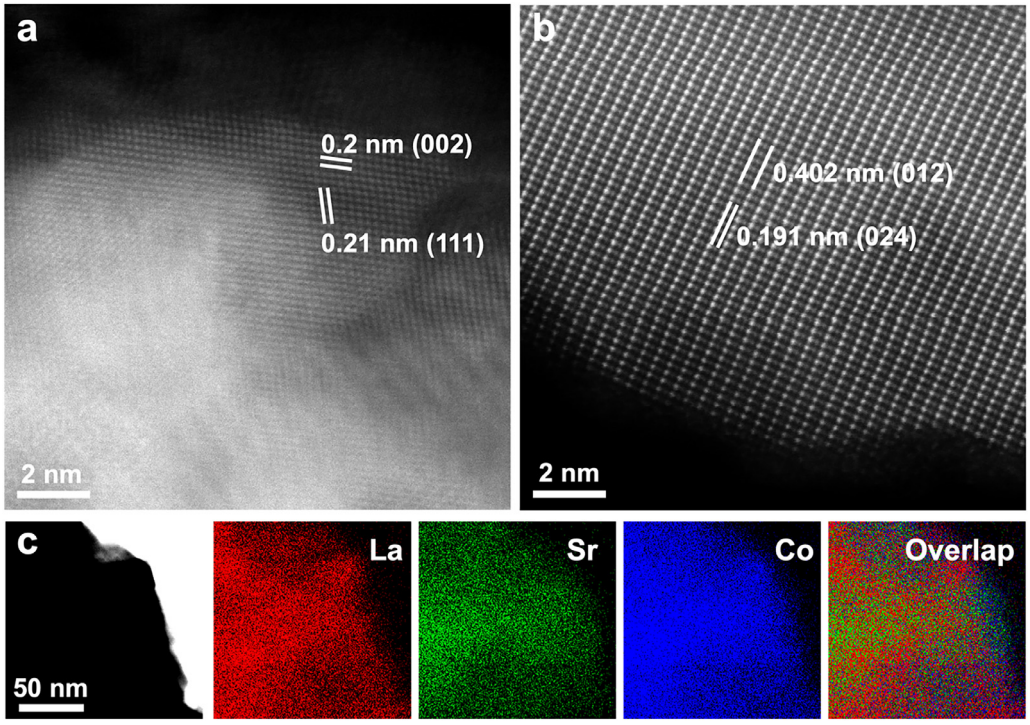

Fig. 2. HAADF-STEM images of (a) orthorhombic $La_{0.6}Sr_{0.4}CoO_3$ (HTS-2), obtained by the HTS method, and (b) hexagonal $La_{0.6}Sr_{0.4}CoO_3$, obtained by muffle furnace calcination. (c) STEM image and the corresponding STEM–EDS elemental mapping of orthorhombic $La_{0.6}Sr_{0.4}CoO_3$ (HTS-2).

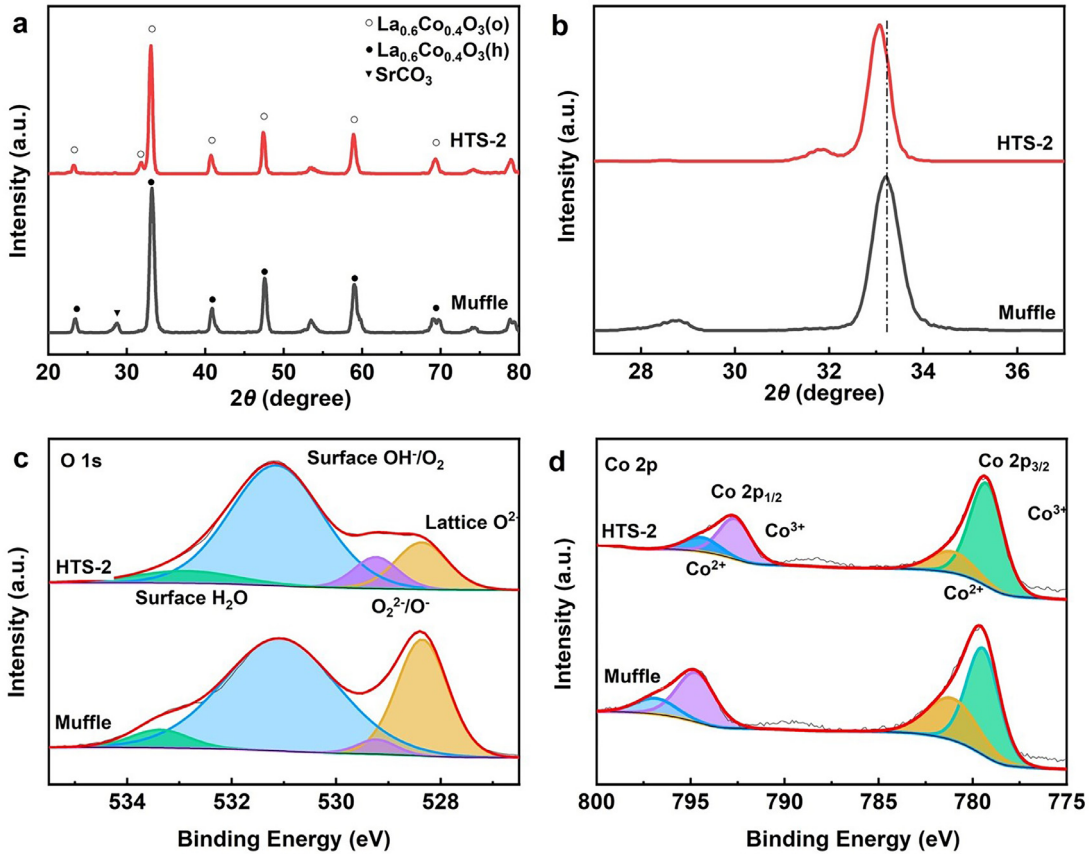

Fig. 3. (a) the XRD patterns; (b) the enlarged XRD patterns from 25° to 40°; the XPS spectra of (c) O 1s; (d) Co 2p of sample HTS-2 and Muffle, respectively.

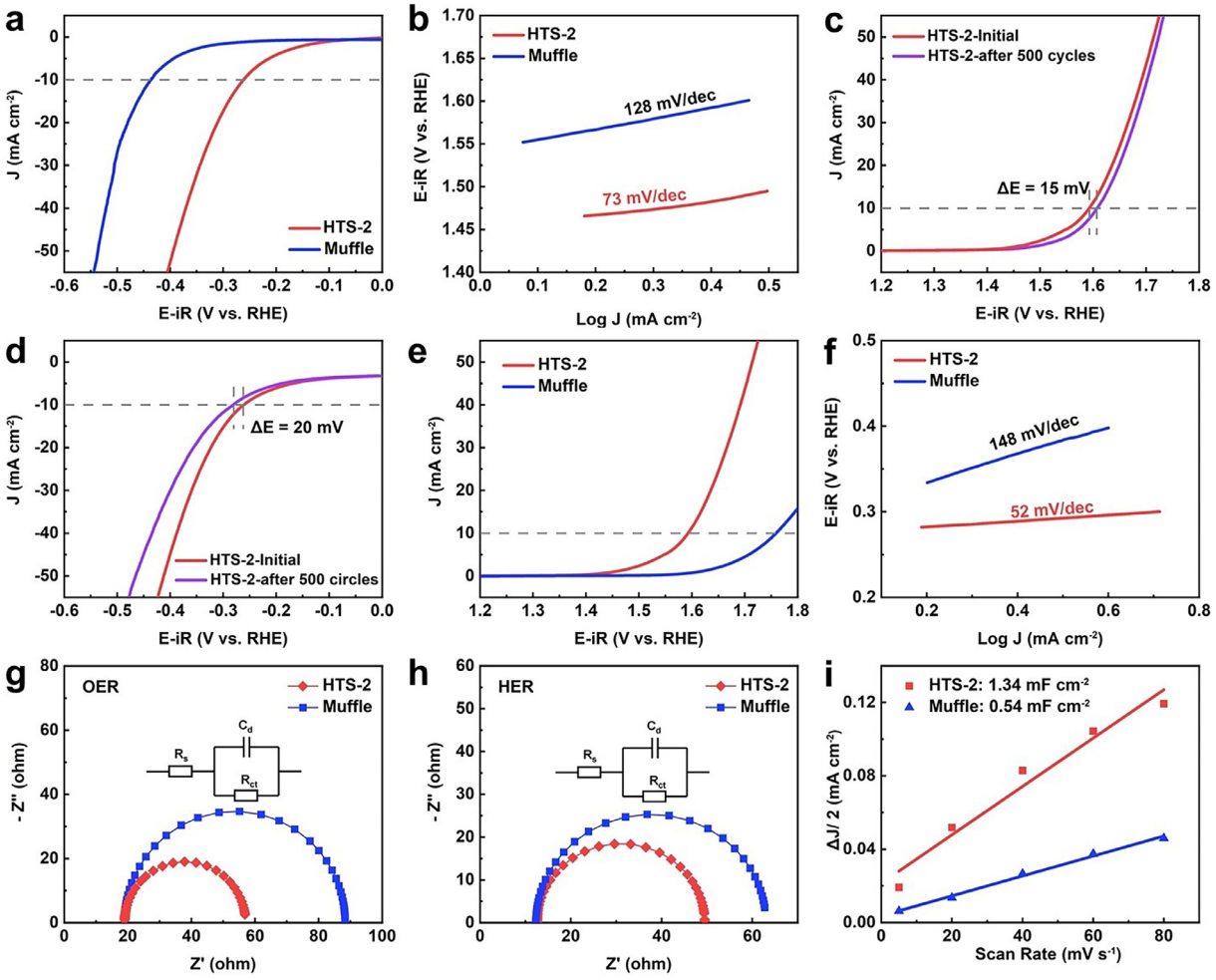

Fig. 4. OER tests: (a) LSV curves; (b) the corresponding Tafel plots of sample HTS-2 and Muffle; (c) cyclic stability curves of HTS-2. HER tests: (d) LSV curves; (e) the corresponding Tafel plots of sample HTS-2 and Muffle; (f) cyclic stability curves of HTS-2. EIS spectra of (g) OER (h) HER and (i) capacitive currents of sample HTS-2 and Muffle.

X-ray photoelectron spectroscopy (XPS) was used to investigate the structure of $La_{0.6}Sr_{0.4}CoO_3$ (Fig. 3 (c, d)). As shown in Fig. 3(c), the peaks of O 1s may be separated into four peaks (i.e., 528.9, 529.6, 531.3, and 532.9 eV) for subsequent identification [15]. The species of surface O 1s are indexed as O^{2-} (lattice oxygen), O_2^{2-}/O^- (highly oxidative oxygen), $-OH/O_2$ (surface absorbed oxygen or hydroxyl) and H_2O (surface absorbed water), respectively. The percentage of each kind of surface O 1s could be calculated according to the area of the peaks (Table S2). It was reported that a higher ratio of highly oxidative oxygen or surface-absorbed oxygen/hydroxyl would bring more oxygen vacancies [46]. The absorbed O_2 on the surface can strengthen the bond between B-site cations and oxygen, and then motivate the charge transfer during the catalytic process. In addition, more hydroxyl groups could facilitate the combination of O–O in OOH^-, so as to promote the performance of OER. According to the calculation results, HTS-2 exhibited larger concentrations for both oxygen species of O_2^{2-}/O^- (8.61 %) and $-OH/O_2$ (68.96 %) than that obtained by traditional calcination (Muffle).

For the Co 2p spectra, the distinct peaks located at 780.0 eV (Co $2p_{1/2}$) and 795.0 eV (Co $2p_{3/2}$) may be divided into four peaks, which are denoted as Co^{3+} (780.3 and 795.0 eV) and Co^{2+} (781.8 and 796.9 eV) [47,48]. Moreover, the ratio of Co^{3+}/Co^{2+} and the average valence state of Co ions were calculated according to the peak area (Table S3). It has been pointed out in previous research that Co^{2+} could be assumed as high spin (HS, $2e_g\uparrow3t_{2g}\uparrow2t_{2g}\downarrow$), while Co^{3+} as intermediate spin (IS, $e_g\uparrow3t_{2g}\uparrow2t_{2g}\downarrow$) [8,49]. Taking e_g orbital filling as the description character of the electrochemical activity of perovskite oxides, when e_g occupancy on B-site cations is closer to 1.2, the catalysts show better performance for OER and HER [50]. In our experiment, Co ions are the B-site cations, so the value of e_g orbital filling could be calculated according to the following equation: $e_g = (1 \times Co^{3+}/Co^{2+} + 2 \times 1)/(Co^{3+}/Co^{2+} + 1)$. The e_g occupancy is listed in Table S3. By comparison, the value of e_g occupancy for HTS-2 was closer to 1.2 than that for the sample obtained by the Muffle furnace calcination method, indicating the higher performance of HTS-2.

2.2. Electrochemical performances

An electrocatalytic OER test was carried out using the three-electrode cell in 1 mol L^{-1} KOH aqueous solution, as presented in Fig. 4(a–c). The potentials of the reference electrode were normalized to a reversible hydrogen electrode (RHE) at room temperature. From the linear sweep voltammetry (LSV) polarization curves of OER at the scan rate of 5 mV s^{-1} (Fig. 4(a)), HTS-2 showed enhanced electrocatalytic activity with a low overpotential of 363 mV at 10 mA cm^{-2}, as compared to the Muffle. The Tafel slope for HTS-2 is 73 mV dec^{-1} (Fig. 4(b)), which is also lower than that of the Muffle (128 mV dec^{-1}), suggesting fast kinetics of HTS-2. The mass activities are calculated based on the ratio of current and mass loading under a certain voltage. HTS-2 showed surpassed mass activity over the Muffle, which was 103.2 and 10.6 A g^{-1}, respectively,

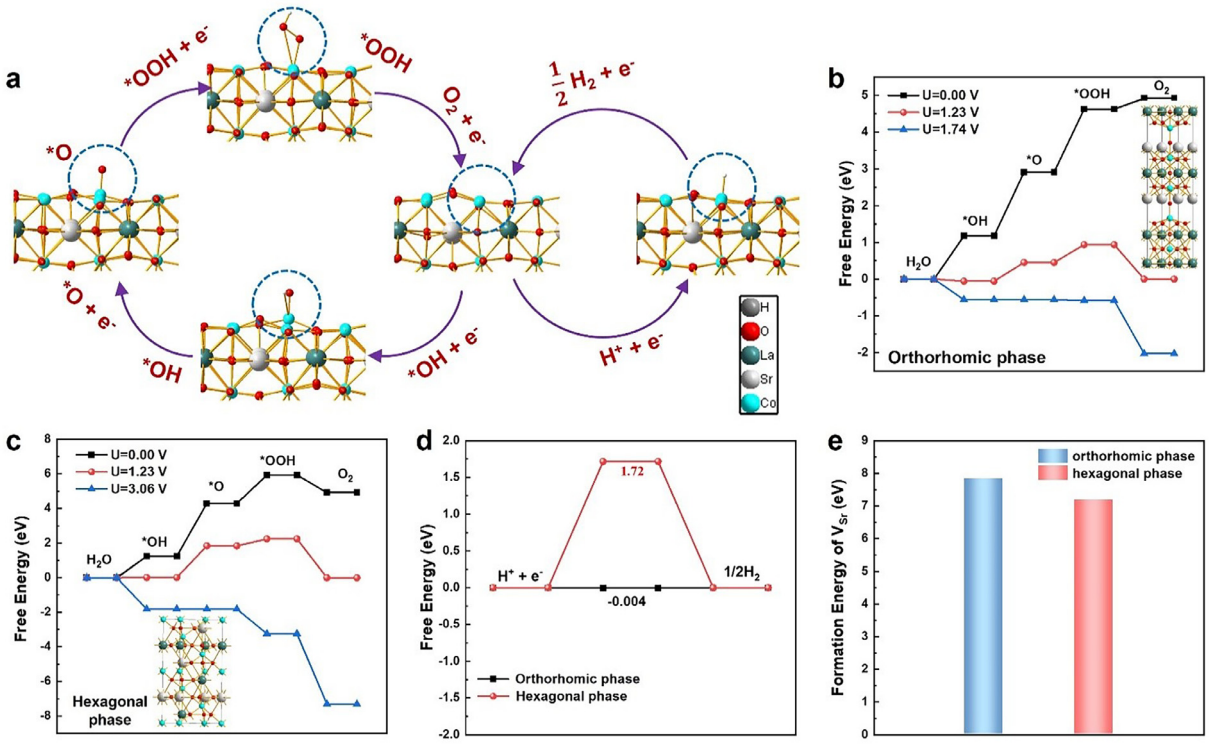

Fig. 5. (a) Water splitting cycle diagram for orthorhombic $La_{0.6}Sr_{0.4}CoO_3$ at the Co site. Free energy and pathways of OER for the reconstruction models of (b) orthorhombic and (c) hexagonal $La_{0.6}Sr_{0.4}CoO_3$ at Co site, respectively. (d) Free energy of HER for orthorhombic and hexagonal $La_{0.6}Sr_{0.4}CoO_3$. (e) The formation energy of Sr deficiency of orthorhombic and hexagonal $La_{0.6}Sr_{0.4}CoO_3$.

at a potential of 1.7 V (vs. RHE). Moreover, the TOF_{mass} for the HTS-2 and Muffle were 0.061 and 0.006 s^{-1} at 1.7 V vs. RHE, respectively (Fig. S5(a)). HTS-2 still shows a greater turnover frequency, almost 10 times than that of Muffle. Fig. 4(c) displays the reduction in performance after 500 cycles of cyclic voltammetry test at the scan rate of 50 mV s^{-1}, showing an overpotential gap of about 15 mV.

Therefore, HTS-2 exhibits a nice OER durability.

To evaluate the electrocatalytic HER performance of the orthorhombic $La_{0.6}Sr_{0.4}CoO_3$ in O_2-saturated 1 mol L^{-1} KOH aqueous solution, the Muffle calcinated $La_{0.6}Sr_{0.4}CoO_3$ was selected as a reference catalyst, with all potentials normalized to the RHE. The LSV polarization curves recorded at a scan rate of 5 mV s^{-1} and the exact overpotential were shown in Fig. 4(d, e). The overpotential of the HTS-2 at −10 mA cm^{-2} is 261 mV, which is better than that of the Muffle (436 mV). To gain more insight into the kinetics of HER, further analysis of the Tafel slope was performed. As shown in Fig. 4(e), the HTS-2 displayed a smaller Tafel slope (52 mV dec^{-1}) compared to Muffle (148 mV dec^{-1}), indicating more efficient HER kinetics of HTS-2. Moreover, the mass activity and TOF_{mass} of HTS-2 are −36.1 A g^{-1} and −0.042 s^{-1} (both at –0.3 V vs. RHE), respectively, which are distinctively higher than those of the Muffle (Fig. S5(b)). In Fig. 4(f), HTS-2 showed a slight increase in 20 mV in the overpotential at –10 mA cm^{-2} after 500 cycles, indicating the fine stability of HTS-2 for HER. In addition, the overpotential of HTS-2 is comparable to or even smaller than those of the reported perovskite electrocatalysts (Table S4). Given the above analysis, it is demonstrated that the HTS strategy could produce perovskite oxides with high purity and good electrocatalytic performance.

2.3. Discussion

Electrochemical impedance spectra (EIS) of OER and HER are demonstrated in Fig. 4(g, h). The semicircles of Nyquist plots represent the charge-transferring resistance, and a smaller diameter indicates lower resistance. The charge transfer resistance of HTS-2 is found to be 37 Ω for OER (Fig. 4(g)) and 35 Ω for HER (Fig. 4(h)), which are smaller than those of the Muffle. The low resistance ensures a fast charge-transfer rate, which is likely the reason for the good electrochemical activity of HTS-2.

The cyclic voltammetry tests of the HTS-2 and Muffle were conducted using various scan rates (i.e., 5, 20, 40, 60, and 80 mV s^{-1}) within a potential range of 1.1–1.3 V (vs. RHE). The resulting curves were analyzed and categorized into five patterns in Fig. S6. The double layer capacitance (C_{dl}) of the samples was determined using the formula: $\Delta i/2 = \nu \times C_{dl}$, where ν is the scan rate and the current (i) was selected from the medium voltage (1.20 V vs. RHE). The C_{dl} values for the catalysts were plotted in Fig. 4(i) and were found to be 1.34 mF cm^{-2} (HTS-2) and 0.54 mF cm^{-2} (Muffle), respectively. The C_{dl} value is typically used to determine the electrochemical active surface area (ECSA) of catalysts, with larger values indicating a greater number of active sites on the surface. Therefore, the ECSA of the HTS-2 is larger than that of the Muffle. This suggests that HTS-2 will perform better in electrocatalytic tests due to the presence of more active sites on the surface.

To elucidate the reaction mechanism of the hydrolysis reaction on orthorhombic (ort-) and hexagonal phase (hcp-) $La_{0.6}Sr_{0.4}CoO_3$ (LSCO), the theoretical calculation based on density functional theory (DFT) was employed to explore the OER and HER processes (see Supporting information for the detailed calculation process). The electrocatalytic cycle mechanism for OER and HER is schematically illustrated in Fig. 5(a). Based on the ort- and hcp-LSCO phases, the ort-LSCO(001) and hcp-LSCO(012) were employed as the active surfaces where the Co and O will be exposed. According to the D-band center theory supposed by Norskov' group [51], the d orbital of transition metal will mainly contribute to the adsorption of the intermediate and the catalytic reaction. Therefore,

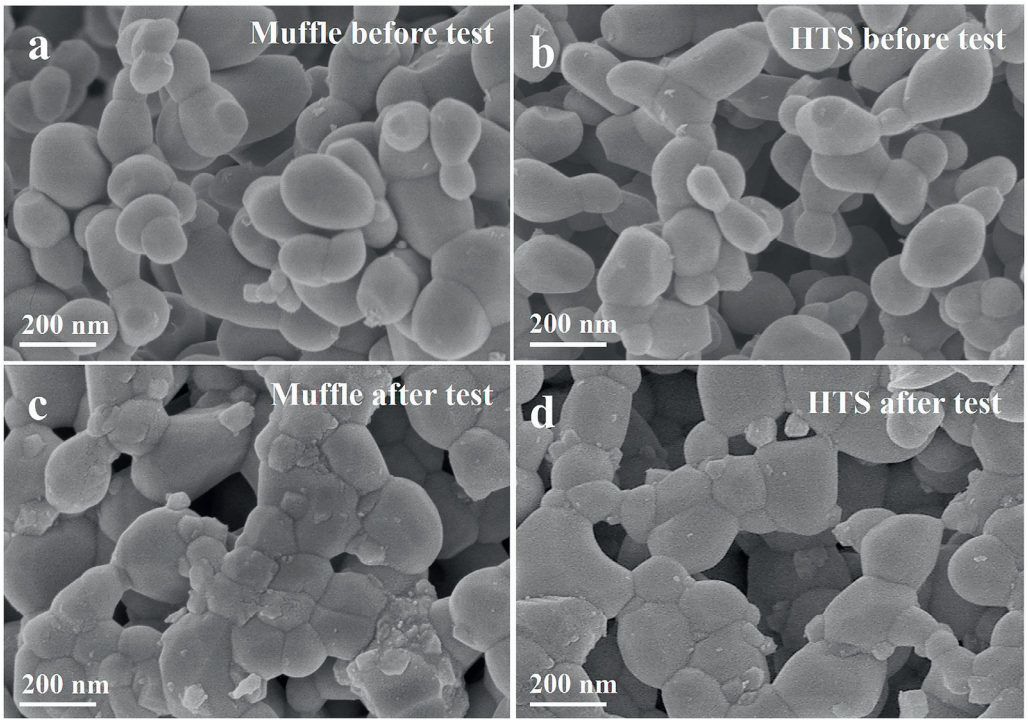

Fig. 6. SEM images of HTS-2 and Muffle before and after stability tests.

for both ort-LSCO(001) and hcp-LSCO(012), the Co atom should be the active center. The free energy curves of OER and HER are investigated (Fig. 5(b–d)) to estimate the activity of the hydrolysis reaction. For the OER process, it is seen that the lowest potential U to turn all the protonation process to be exothermic is 1.74 V (Fig. 5(b)) on ort-LSCO(001), which is closer to the equilibrium potential of 1.23 V than that of hcp-LSCO(012) (U = 3.06 V) (Fig. 5(c)). Meanwhile, for HER, the free energy change on ort-LSCO(001) (ΔG_H = −0.004 eV) is very close to 0 eV, compared with hcp-LSCO(012) (ΔG_H = 1.72 eV), as shown in Fig. 5(d). These results indicate that ort-LSCO(001) will show higher OER and HER activity than that of hcp-LSCO(012), which aligns well with the experimental observations. Additionally, ort-LSCO(001) shows a higher formation energy of Sr deficiency (7.84 eV) than that of hcp-LSCO(012) (7.19 eV), suggesting that the Sr losing will be suppressed on the former system (Fig. 5(e)).

Moreover, the energy-level diagram was investigated by theoretical calculation. It is revealed that the Fermi levels of ort and hcp-LSCO are below the LUMO energy level of H_2O (Fig. S7), indicating that the H_2O dissociation cannot be dissociation spontaneously. This observation suggests that spontaneous dissociation of H_2O molecules is not feasible. Consequently, the process of H_2O splitting must be realized by extra energy, such as external potential. When an external potential is applied, the energy of free electrons is increased, enabling them to reach the high energy level of H_2O-LUMO, thereby activating the H_2O molecules. This enhanced charge/electron transition serves to facilitate the process of H_2O splitting when external potential is applied.

The samples including the HTS-2 and the Muffle were characterized by SEM before and after the stability tests (Fig. 6). The pristine HTS-2 and Muffle samples exhibited uniform particle distribution, with smooth surfaces and well-stratified, porous structures (Fig. 6(a, b)). However, after the cyclic tests, the morphology of the Muffle changed significantly (Fig. 6(c)), with insulating phases forming on the surface. This might be due to the Sr segregation occurring in the electrochemical circulations [52], which is a common phenomenon in the application of perovskite oxides containing strontium. As Sr segregation can interfere with the electronic exchange process, it may cause a decrease in electrocatalytic properties [52,53]. Previous research has reported that an orthorhombic structure can reduce the Sr segregation in perovskites [53]. In this work, the structure of HTS-2 maintained well after the stability test (Fig. 6(d)), indicating that the orthorhombic structure produced by the HTS method could suppress Sr segregation in LSC during operation, thereby improving the electrochemical performance.

XPS results provide insights into the surface composition of the samples. The contents of the three kinds of metal atoms of HTS-2 and Muffle are listed in Table S5. The atomic percentages of strontium were initially 21.97 % (HTS-2) and 20.05 % (Muffle). After the durability tests, the Sr percentage in Muffle increased to 32.31 %, whereas the Sr element in HTS-2 only exhibited a slight increase. This indicates that Sr segregation was largely suppressed in HTS-2, consistent with the analysis presented in Fig. 6.

3. Conclusions

In summary, $La_{0.6}Sr_{0.4}CoO_3$ perovskite oxides were successfully prepared using the HTS technique with mixed metal nitrates as precursors. Compared to the sample obtained by the traditional Muffle furnace calcination method, the $La_{0.6}Sr_{0.4}CoO_3$ perovskite oxides (HTS-2) prepared using HTS (Joule heating for 2 min) method showed high purity with the presence of orthorhombic phase and exhibited better OER and HER activities. The good electrocatalytic performance of HTS-2 is mainly attributed to its orthorhombic structure, which suppresses strontium segregation, as well as the higher percentages of highly oxidative oxygen species and absorbed oxygen species on the surface. These factors contribute to the presence of more active sites and lower charge-transfer resistance. This study offers a novel, simple, and rapid method for the synthesis of perovskite oxides with good electro-

chemical performance that surpasses traditional perovskite electrocatalysts.

Declaration of competing interest

The authors declare that they have no known competing financial interests or personal relationships that could have appeared to influence the work reported in this paper.

Acknowledgements

This work was supported by the National Natural Science Foundation of China (Nos. 42277369 and 52171219).

Supplementary materials

Supplementary material associated with this article can be found, in the online version, at doi:10.1016/j.jmst.2023.11.067.

References

[1] S. Chu, A. Majumdar, Nature 488 (2012) 294–303.
[2] N.K. Chaudhari, H. Jin, B. Kim, K. Lee, Nanoscale 9 (2017) 12231–12247.
[3] Y. Zheng, Y. Jiao, Y. Zhu, Q. Cai, A. Vasileff, L.H. Li, Y. Han, Y. Chen, S.Z. Qiao, J. Am. Chem. Soc. 139 (2017) 3336–3339.
[4] Z. Wang, S. Yuan, T. Zang, T. Li, Y. Zhou, J. Liu, T. Liu, K. Wang, Q. Wang, J. Mater. Sci. Technol. 142 (2023) 144–151.
[5] M. Jahan, Z. Liu, K.P. Loh, Adv. Funct. Mater. 23 (2013) 5363–5372.
[6] M. Tahir, L. Pan, F. Idrees, X. Zhang, L. Wang, J.J. Zou, Z.L. Wang, Nano Energy 37 (2017) 136–157.
[7] Z. Zhang, Y. Chen, Z. Dai, S. Tan, D. Chen, Electrochim. Acta 312 (2019) 128–136.
[8] Y. Zhu, W. Zhou, Y. Zhong, Y. Bu, X. Chen, Q. Zhong, M. Liu, Z. Shao, Adv. Energy Mater. 7 (2017) 1602122.
[9] X. Ji, F. Yang, Y. Du, J. Li, J. Li, Q. Hu, J. Mater. Sci. Technol. 168 (2024) 71–78.
[10] Z. An, H. Xue, J. Sun, N. Guo, T. Song, J. Sun, Y.R. Hao, Q. Wang, Chin. J. Struct. Chem. 41 (2022) 2208037–2208043.
[11] J. Feng, F. Lv, W. Zhang, P. Li, K. Wang, C. Yang, B. Wang, Y. Yang, J. Zhou, F. Lin, Adv. Mater. 29 (2017) 1703798.
[12] Z. Jian, P. Liu, F. Li, P. He, X. Guo, M. Chen, H. Zhou, Angew. Chem. Inter. Ed. 53 (2014) 442–446.
[13] M. Lebid, M. Omari, Synthesis and electrochemical properties of LaFeO3 oxides prepared via sol–gel method, Arab. J. Sci. Eng. 39 (1) (2014) 147–152.
[14] N.T. Suen, S.F. Hung, Q. Quan, N. Zhang, Y.J. Xu, H.M. Chen, Chem. Soc. Rev. 46 (2017) 337–365.
[15] Y. Da, L. Zeng, C. Wang, C. Gong, L. Cui, Electrochim. Acta 300 (2019) 85–92.
[16] J. Hu, Q. Liu, L. Shi, Z. Shi, H. Huang, Appl. Surf. Sci. 402 (2017) 61–69.
[17] Z. Wang, C. Chen, C. Feng, J. Wang, B. Zou, M. Zhao, F. Wu, Acta Phys. Chim. Sin. 24 (2008) 375–378.
[18] Y. Wang, L. Wang, K. Zhang, J. Xu, Q. Wu, Z. Xie, W. An, X. Liang, X. Zou, Chin. J. Catal. 50 (2023) 109–125.
[19] D. Mierwaldt, V. Roddatis, M. Risch, J. Scholz, J. Geppert, M.E. Abrishami, C. Jooss, Adv. Sustain. Syst. 1 (2017) 1700109.
[20] C. Wang, L. Zeng, W. Guo, C. Gong, J. Yang, RSC Adv. 9 (2019) 35646–35654.
[21] Z. Wang, Y. You, J. Yuan, Y.X. Yin, Y.T. Li, S. Xin, D. Zhang, ACS Appl. Mater. Interfaces 8 (2016) 6520–6528.
[22] D. Zhen, B. Zhao, H.C. Shin, Y. Bu, Y. Ding, G. He, M. Liu, Adv. Mater. Interfaces 4 (2017) 1700146.
[23] S. Song, J. Zhou, J. Sun, S. Zhang, X. Lin, Z. Hu, J. Hu, L. Zhang, J.Q. Wang, Chin. J. Catal. 41 (2020) 592–597.
[24] K. Liu, J. Li, Q. Wang, X. Wang, D. Qian, J. Jiang, J. Li, Z. Chen, J. Alloy. Compd. 725 (2017) 260–269.
[25] L. Yu, N. Xu, T. Zhu, Z. Xu, M. Sun, D. Geng, Int. J. Hydrog. Energy 45 (2020) 30583–30591.
[26] F. Lu, Y. Wang, C. Jin, F. Li, R. Yang, F. Chen, J. Power Sources 293 (2015) 726–733.
[27] X. Xu, Y. Pan, W. Zhou, Y. Chen, Z. Zhang, Z. Shao, Electrochim. Acta 219 (2016) 553–559.
[28] B. Hua, M. Li, Y.Q. Zhang, Y.F. Sun, J.L. Luo, Adv. Energy Mater. 7 (2017) 1700666.
[29] Y. Chen, G.C. Egan, J. Wan, S. Zhu, R.J. Jacob, W. Zhou, J. Dai, Y. Wang, V.A. Danner, Y. Yao, Nat. Commun. 7 (2016) 12332.
[30] S. Liu, Z. Hu, Y. Wu, J. Zhang, Y. Zhang, B. Cui, C. Liu, S. Hu, N. Zhao, X. Han, Adv. Mater. 32 (2020) 2006034.
[31] X. Wang, Q. Dong, H. Qiao, Z. Huang, M.T. Saray, G. Zhong, Z. Lin, M. Cui, A. Brozena, M. Hong, Adv. Mater. 32 (2020) 2002853.
[32] S. Dou, J. Xu, X. Cui, W. Liu, Z. Zhang, Y. Deng, W. Hu, Y. Chen, Adv. Energy Mater. 10 (2020) 2001331.
[33] S. Liu, Y. Shen, Y. Zhang, B. Cui, S. Xi, J. Zhang, L. Xu, S. Zhu, Y. Chen, Y. Deng, Adv. Mater. 34 (2022) 2106973.
[34] Y. Li, Y. Chen, A. Nie, A. Lu, R.J. Jacob, T. Gao, J. Song, J. Dai, J. Wan, G. Pastel, Adv. Energy Mater. 7 (2017) 1601783.
[35] Y. Chen, K. Fu, S. Zhu, W. Luo, Y. Wang, Y. Li, E. Hitz, Y. Yao, J. Dai, J. Wan, Nano Lett. 16 (2016) 3616–3623.
[36] Y. Chen, Y. Li, Y. Wang, K. Fu, V.A. Danner, J. Dai, S.D. Lacey, Y. Yao, L. Hu, Nano Lett. 16 (2016) 5553–5558.
[37] C. Yang, Y. Yao, S. He, H. Xie, E. Hitz, L. Hu, Adv. Mater. 29 (2017) 1702714.
[38] F. Chen, Y. Yao, A. Nie, S. Xu, J. Dai, Y.Li E.Hitz, A. Lu, Z. Huang, T. Li, Adv. Energy Mater. 8 (2018) 1800466.
[39] Y. Li, T. Gao, Y. Yao, Z. Liu, Y. Kuang, C. Chen, J. Song, S. Xu, E.M. Hitz, B. Liu, Adv. Energy Mater. 8 (2018) 1801289.
[40] C. Yang, M. Cui, N. Li, Z. Liu, S. Hwang, H. Xie, X. Wang, Y. Kuang, M. Jiao, D. Su, Nano Energy 63 (2019) 103855.
[41] H. Xie, K. Fu, C. Yang, Y. Yao, J. Rao, Y. Zhou, B. Liu, D. Kirsch, L. Hu, Small Methods 2 (2018) 1700371.
[42] Y. Chen, S. Xu, Y. Li, R.J. Jacob, Y. Kuang, B. Liu, Y. Wang, G. Pastel, L.G. Salamanca-Riba, M.R. Zachariah, Adv. Energy Mater. 7 (2017) 1700482.
[43] Y. Chen, S. Xu, S. Zhu, R.J. Jacob, G. Pastel, Y. Wang, Y. Li, J. Dai, F. Chen, H. Xie, Nano Res. 12 (2019) 2259–2267.
[44] W. Zhu, J. Zhang, J. Luo, C. Zeng, H. Su, J. Zhang, R. Liu, E. Hu, Y. Liu, W.D. Liu, Adv. Mater. 35 (2023) 2208974.
[45] S. Ponce, M. Pena, J. Fierro, Appl. Catal. B-Environ. 24 (2000) 193–205.
[46] C. Su, W. Wang, Y. Chen, G. Yang, X. Xu, M.O. Tadé, Z. Shao, ACS Appl. Mater. Interfaces 7 (2015) 17663–17670.
[47] Y. Wu, L. Li, B. Chu, Y. Yi, Z. Qin, M. Fan, Q. Qin, H. He, L. Zhang, L. Dong, Appl. Catal. A-Gen. 568 (2018) 43–53.
[48] L. Zeng, L. Cui, C. Wang, W. Guo, C. Gong, J. Hazard. Mater. 383 (2020) 121210.
[49] W.G. Hardin, D.A. Slanac, X. Wang, S. Dai, K.P. Johnston, K.J. Stevenson, J. Phys. Chem. Lett. 4 (2013) 1254–1259.
[50] J. Suntivich, K.J. May, H.A. Gasteiger, J.B. Goodenough, Y. Shao-Horn, Science 334 (2011) 1383–1385 (1979).
[51] A. Ruban, B. Hammer, P. Stoltze, H.L. Skriver, J.K. Nørskov, J. Mol. Catal. A-Chem. 115 (1997) 421–429.
[52] W. Guo, L. Cui, H. Xu, C. Gong, Appl. Surf. Sci. 529 (2020) 147165.
[53] Y. Yang, H. Bao, H. Ni, X. Ou, S. Wang, B. Lin, P. Feng, Y. Ling, J. Power Sources 482 (2021) 228959.